The 1884 Andalusian Earthquake, Spain: Re-evaluation of Seismic Intensities and Source Determination

Elisa Buforn[*1], Javier Fernández-Fraile[2], Simone Cesca[3], Carlos Sanz de Galdeano[4], José Manuel Martínez-Solares[2], Agustín Udías[1], Maurizio Mattesini[1], and David Márquez-Reviriego[1]

Abstract

In this work, we present a quantified model of the seismic source for the 1884 Andalusian earthquake (Granada, Spain) that accounts for the dimensions and orientation of the rupture, average slip, focal depth, magnitude, and scalar seismic moment. We undertook archival research to find additional accounts, increasing the number of intensity data points from 157 to 213, which has allowed for a more detailed distribution of European Macroseismic Scale 1998 intensities. The re-evaluated intensity values were converted into peak ground acceleration (PGA) values using an empirical relation and then modeled using rectangular fault models with regular slip and different fault sizes, depths, and geometries. We have used two different approaches to carry out the comparison between synthetic and observed PGAs. The best results correspond to a normal fault with strikes of 270°–330° that steeply dips to the north, with the northern block moving down, and a shallow focus. This geometry agrees with that of the Ventas de Zafarraya fault system, which was proposed by different authors as the origin of the 1884 earthquake.

Cite this article as Buforn, E., J. Fernández-Fraile, S. Cesca, C. Sanz de Galdeano, J. M. Martínez-Solares, A. Udías, M. Mattesini, and D. Márquez-Reviriego (2025). The 1884 Andalusian Earthquake, Spain: Re-evaluation of Seismic Intensities and Source Determination, *Seismol. Res. Lett.* **96**, 3523–3540, doi: 10.1785/0220250036.

Supplemental Material

Introduction

On 25 December 1884, a violent earthquake struck southern Spain, causing severe damage to towns and villages in the regions of Granada and Málaga (Fig. 1, see Data and Resources). According to the Instituto Geográfico Nacional (IGN) online catalog, the maximum intensity (I_{max}) was IX–X at the European Macroseismic Scale 1998 (EMS-98; Grünthal, 1998), and the moment magnitude M_w 6.7–7.0 (see Data and Resources). Total estimations of casualties and damage are: 839 people died, more than 1500 reported injuries, 4400 buildings destroyed, and more than 13,000 buildings damaged (see Data and Resources; Udías *et al.*, 2022). Many aftershocks followed until April 1885 (Udías and Muñoz, 1979). The 1884 earthquake, also known as the Andalusian earthquake, was the last earthquake to cause severe damage in Spain. During the twentieth century and the beginning of the twenty-first century, seismic activity in Spain was low, that is, somewhat less than that in the previous centuries. The largest earthquakes ($M_w > 7$) in this period occurred offshore (the 1969 event that occurred southwest of Saint Vincent Cape, Buforn *et al.*, 2020) or had deep foci (h = 650 km, the 1954 Granada deep earthquake; Buforn *et al.*, 2011), resulting in moderate or no damage.

The 1884 Andalusian earthquake attracted great interest from the European scientific community, with 58 books and articles published during 1885 in Spain, France, Italy, Germany, and Great Britain (Udías *et al.*, 2022). For the first time in Europe, three commissions were established (in Spain, France, and Italy) to study the nature and effects of the earthquake. Some of the best experts and scientists in the fields of geology and seismology, such as G. Mercalli and T. Taramelli (Italian Commission) and F. Fouqué (French Commission), who visited the epicentral area and wrote detailed reports, participated in these commissions. An important part of the Spanish Commission's report was a survey with 33 questions distributed to the population, which received 500 responses (Fernández de Castro *et al.*, 1885). The work of the French Commission focused on regional geology and surveyed villages with great damage and ground effects, defining the epicentral area and suggesting a focal depth of 11 km (Fouqué, 1889b). The Italian Commission's report included one of the first intensity maps and a detailed study of the seismicity of the region (Taramelli and Mercalli, 1885). Among the Spanish publications, the expanded report

1. Dpt. Física de la Tierra y Astrofísica, Universidad Complutense, Madrid, Spain, https://orcid.org/0000-0002-0846-8199 (EB); https://orcid.org/0000-0002-7744-8626 (MM); 2. Instituto Geográfico Nacional (IGN), Madrid, Spain, https://orcid.org/0000-0003-2811-8898 (JF-F); 3. Helmholtz-Zentrum Potsdam (GFZ), Deutsches GeoForschungsZentrum GFZ, Postdam, Germany, https://orcid.org/0000-0001-9419-3904 (SC); 4. Former member of the IACT, Universidad de Granada – CSIC, Granada, Spain, https://orcid.org/0000-0002-3256-7648 (CSG)

*Corresponding author: ebufornp@ucm.es

Figure 1. Damage caused by the 1884 earthquake at Alhama de Granada (see Data and Resources).

by Orueta y Duarte (1885) describes early post-seismic fieldwork, including photographs of damage caused by the earthquake. As a result of these contemporary field investigations, there is abundant contemporary documentation on the damage and ground effects of the earthquake.

Modern reassessments of the earthquake from a seismological viewpoint began with the presentation of an isoseismal map by Steikhardt (1932), which was reproduced by Galbis (1932). Udías and Muñoz (1979) estimated the origin time at 21:08 (UTC), the epicentral coordinates at 36.95° N, 3.98° W (Fig. S1, available in the supplemental material to this article), and the focal depths at 10–20 km; in addition, an isoseismal map was generated (I_{max}IX – X, Medvedev–Sponheuer–Karnik scale, Medvedev *et al.*, 1964). They estimated the magnitude, based on the maximum intensity as **M** 6.7–7.0; the authors proposed a complex source model involving a system of faults with lengths of 20–30 km. López-Arroyo *et al.* (1981) studied the effects of the earthquake on the ground and buildings. Vidal (1986) presented an isoseismal map similar to that of Udías and Muñoz (1979) but with a different distribution of intensity data points (IDPs). Martínez-Solares and Mezcua (2002) re-evaluated the intensities using the EMS-98 scale (Grünthal, 1998), assigning an I_{max} = IX–X, and located the epicenter at 37.00° N, 3.98° W, that is, 5 km north compared with that of Udías and Muñoz (1979; Fig. S1). This epicenter is given as a reference for the 1884 earthquake in the IGN catalog (see Data and Resources). Mezcua *et al.* (2004), using the method of Bakun and Wentworth (1997), estimate a preferred epicenter at 37.05° N, 3.97° W, which is ~5 km northeast of the location proposed by Martínez-Solares and Mezcua (2002), and they give a moment magnitude of M_w 6.5 (Fig. S1).

Recently, a series of studies have been conducted, focusing on geological evidence. Reicherter *et al.* (2003), using paleoseismic data, estimated a rupture length of 16 km on the Ventas de Zafarraya fault (VZF), with vertical normal motion, as the source of the 1884 earthquake, corresponding to a magnitude of **M** 6.4. They mention that an indication of an observed fault rupture, which caused the earthquake, is present on the VZF of approximately 16 km in length divided into two segments. They base their interpretation on two historical references: Douville (1906), which is erroneously referenced, and an anonymous gravure from the University of Berkeley (see Data and Resources) of unknown origin. In fact, Douville (1911), based on Fouqué (1889a,b), referred to rockfalls, landslides, ground collapses, cracks, liquefaction, and changes in the water regime, but not to an observed fault rupture. Rodríguez-Peces *et al.* (2011), from information on the Güevejar landslide triggered by the 1884 earthquake, estimated a minimum value for M_w of 6.5 and attributed its origin to the VZF. Mudarra-Hernández *et al.* (2023) proposed a source model for triggering this earthquake based on possible hydromechanical alterations occurring in deep parts of the VZF. Their study depends greatly on the tectonic model they use; in this case, they used a normal fault that reaches a depth of nearly 10 km. In contrast, Madarieta-Txurruka *et al.* (2024), using geophysical, geodetic, and geological data, proposed a very different model explaining the formation of the VZF as that of a normal fault that formed in the crest of an anticline that cannot reach a great depth.

We considered that the observed macroseismic intensities are the main data available for this earthquake, and any seismic source model for this earthquake must be able to reproduce the direct observations of macroseismic intensities within appreciable uncertainties, as we are proposing here (Lucas *et al.*, 2023). Different approaches have been developed to estimate seismic sources from observed intensities. Hough *et al.* (2005) from the re-evaluated intensity distributions of the 1897 and 1905 earthquakes in north India, together with geodetic constraints on

rupture geometries, obtain maps of theoretically predicted shaking that compare with intensity observations. The difference between predicted and observed shaking is interpreted in terms of site effects. Amplifications of 1–2 intensity units, are roughly an amplification of 2–4 in acceleration. Honoré *et al.* (2011) used synthetic peak ground acceleration (PGA) and peak ground velocity (PGV) values generated using lower-magnitude earthquake records as empirical Green's functions. These authors applied this methodology to the 1660 M_w 6.1 Pyrenees earthquake and noted an underestimation of the predicted intensities due to a possible underestimation of the magnitude of the event. Convertito and Pino (2014) proposed a source model for the 1908 M_w 7.1 Messina, Italy, earthquake based on geodetic data using a model of static slip distribution. The synthetic PGV and PGA values are converted to macroseismic intensities using empirical relationships derived for Italy. The comparison of both the PGA- and PGV-based synthetic macroseismic fields with the original intensities provides tighter constraints for discernment among different source models.

Lozos (2016) used a model of dynamic rupture to show that paleoseismic and historic observations associated with the 1812 **M** ∼ 7.5 California earthquake can be explained by the joint rupture of the San Andreas and San Jacinto faults. In addition, he shows how physics-based modeling can be used for interpreting paleoseismic data sets and understanding prehistoric fault behavior. Griffin *et al.* (2019) used a grid search of earthquake source parameters and ground-motion models (GMMs) to identify possible source mechanisms for damaging historical events in Indonesia. They use a Bayesian inference to characterize uncertainties on the estimation of source parameters. The authors conclude that large intraslab earthquakes have been responsible for major earthquakes that occurred in Java, the 1699 $M_w \sim 7.4$ and the 1867 $M_w \sim 7.8$ events.

Hough and Graves (2020) used a kinematic source model to predict PGA values for the 1933 M_w 6.4 California earthquake for a wide range of rupture models. The authors compare the synthetic PGA values with intensities and strong-motion data available. They obtain the concentration of damage near Compton can be explained by a combination of local site amplification, source-controlled directivity local geology. Martin and Hough (2022) used original sources to re-evaluate the 1860 earthquake sequence in southern Haiti. Intensity inversion and GMMs reveal a complex sequence with three large events (**M** > 6.0): foreshock, mainshock, and a previously unknown damaging earthquake. The authors use GMMs to predict PGAs for a range of rupture models. They conclude that historical earthquakes can be used to explore rupture complexity. Hough *et al.* (2022) studied the 1770 Haiti earthquake, using historical sources and proposed a rupture model quantifying parameters such as fault orientation, dimensions, and stress drop.

Bilham and Hough (2023) proposed an elastic deformation model for the seismic source of the 1886 M_w 7.3 Charleston, United States, earthquake on the basis of the coseismic offset on railroad tracks. This event has a common characteristic with the 1884 Andalusian earthquake, namely, the absence of a documented surface rupture. De Pro-Díaz *et al.* (2023) generated seismic scenarios (in terms of intensities) to localize the fault source for the Málaga 1680 and Dalias 1804 earthquakes, with values for both of I_{max} = VIII–IX, in southern Spain. The results for the Málaga earthquake were not conclusive, but the methodology successfully identified the most likely source for the Dalías earthquake. Munafó *et al.* (2024) studied the 1693 M_w 7.3 Italy earthquake using a stochastic finite-fault simulation approach (Hough *et al.*, 2005) and generated ground-motion scenarios. Using a relationship specific to earthquakes in Italy, the authors obtained intensities that are compared with the observed values, concluding that the observed intensities fit better with those converted from the PGV rather than from the PGA values. Hough and Bilham (2024), from new intensity data for the Charleston 1886 (United States) earthquake, demonstrated the agreement of these observations with the source model proposed by Bilham and Hough (2023), highlighting that the shaking distribution does not strongly constrain the determination of the magnitude.

The aim of our work is to propose a seismic source model for the 1884 earthquake with quantified parameters, that is, the fault-plane orientation, focal depth, fracture dimensions, average slip, scalar seismic moment, and moment magnitude, estimated from a revised distribution of IDPs. A search for new contemporary reports of the damage caused by the earthquake resulted in an increase in the number of IDPs from 157 reported in Martínez-Solares and Mezcua (2002) to 213 reported in this work. In addition, we have re-evaluated some of the already reported data, allowing us to develop an improved shaking intensity map. Using an empirical relation, we have converted the intensity values into PGA values, and from their distribution, we propose a source model of a rectangular fault with uniform slip, giving its orientation (strike, dip, and rake), area (length and width), and slip distribution.

Geological Setting

Many authors associate the 1884 Andalusian earthquake with the fault set of the VZF, which extends in the east–west to west-northwest–east-southeast directions (Figs. 2, 3; Sanz de Galdeano, 1985; Reicherter *et al.*, 2003, Grützner *et al.*, 2013; Madarieta-Txurruka *et al.*, 2024). A short report of the geological setting follows, which helps to understand the proposed source model of the earthquake. The western part (Zafarraya and Ventas sites) of the VZF is situated in the external zone of the Betic Cordillera (Subbetic zone), but eastward, the fault system is located in the internal zone (Fig. 3) as part of the Alpujarran Corridor, in the Betic internal zone (Sanz de Galdeano, 1983; Sanz de Galdeano and Alfaro, 2004). The

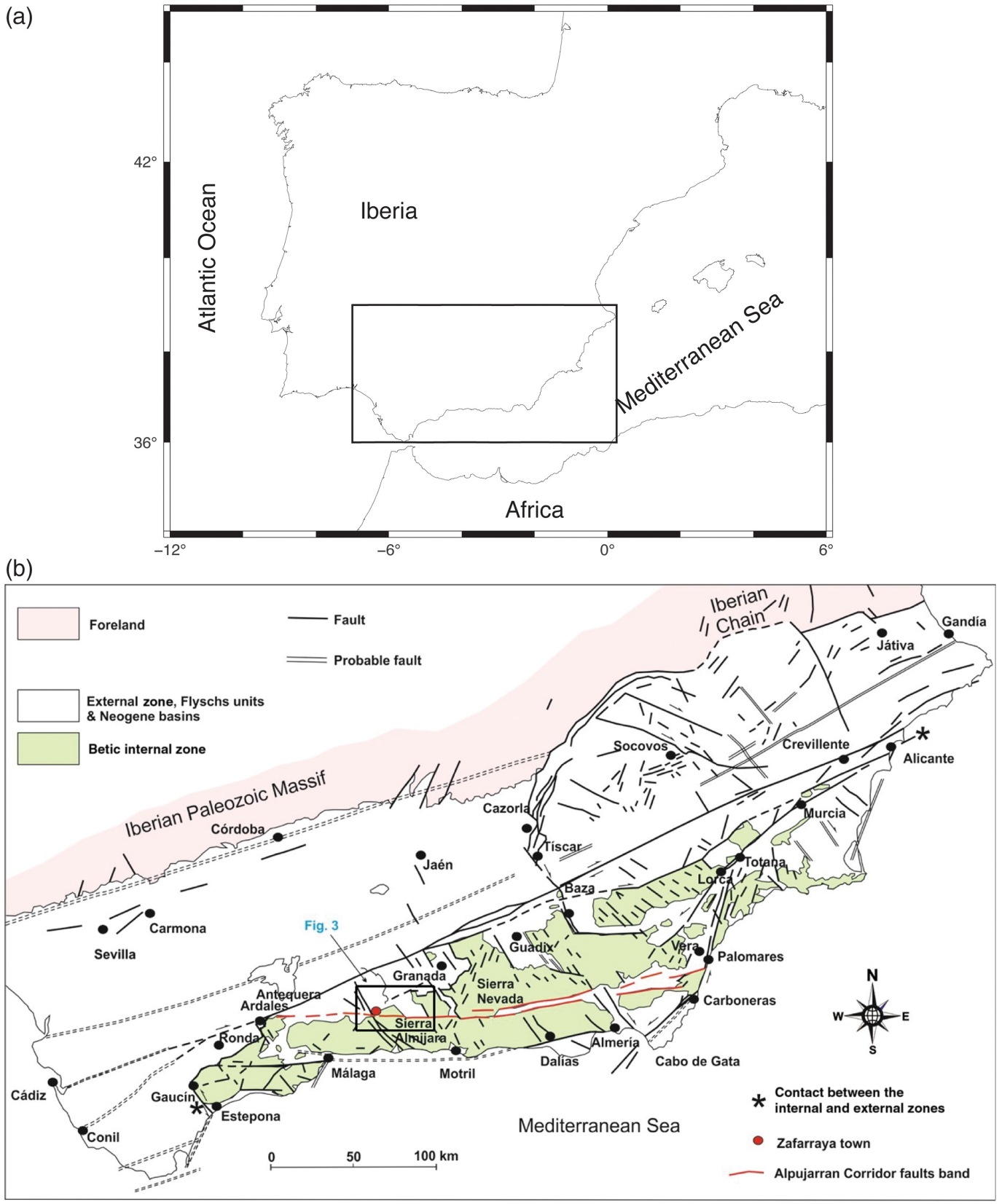

external and internal zones correspond to the main division of the Betic Cordillera. The external zone, which is generally divided into Prebetic and Subbetic zones, corresponds to the Mesozoic and Cenozoic sedimentary cover of the southeast part

Figure 2. (a) Studied region marked by the square. (b) Geological scheme for southern Spain, indicating the main neotectonic and active faults of the Betic Cordillera. The rectangle corresponds to the area shown in Figure 3.

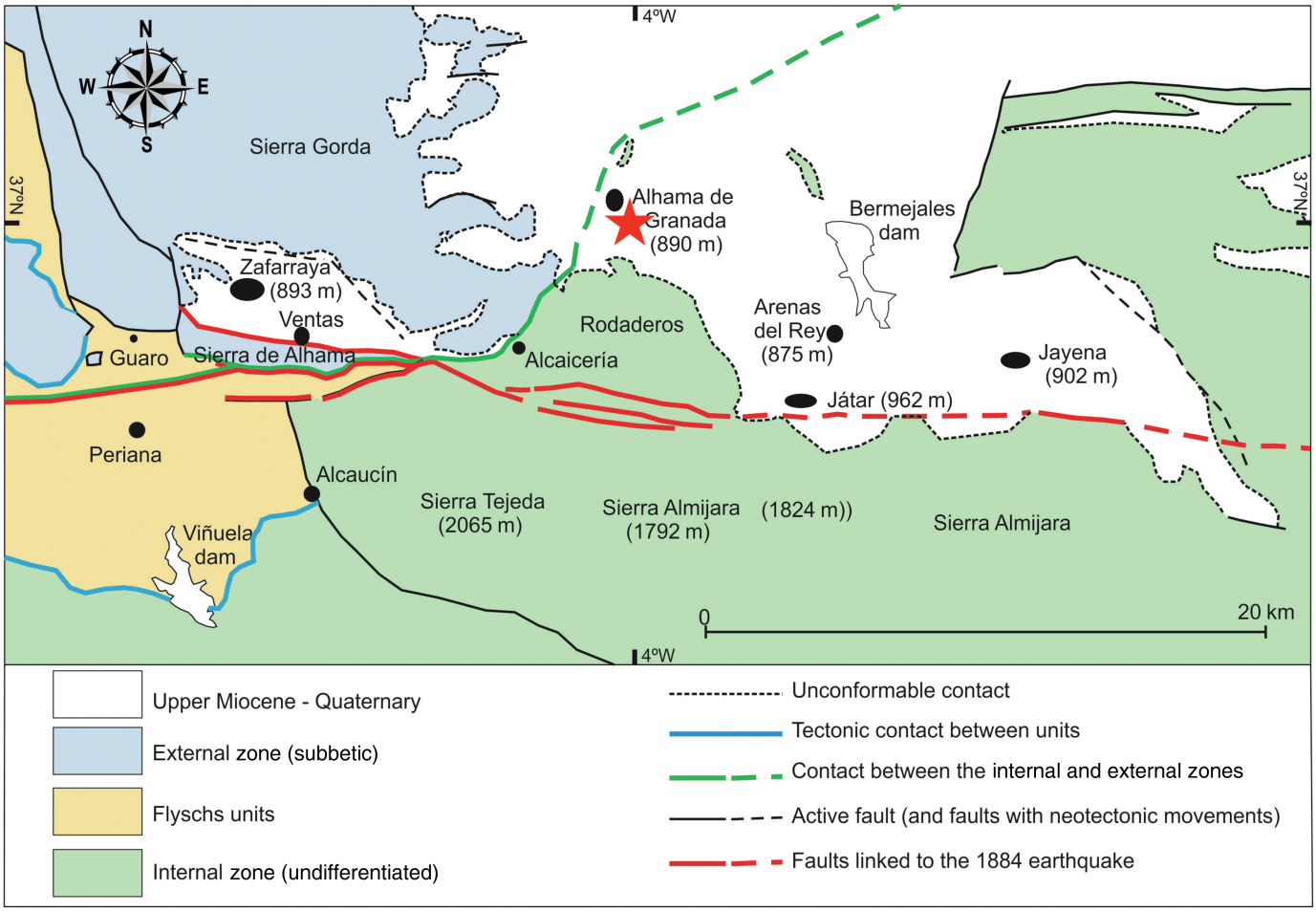

Figure 3. Simplified geologic map of the 1884 epicentral area (the square in Fig. 2b). The red star shows the macroseismic epicenter.

of the Paleozoic Iberian Massif, whereas the internal zone, which formed hundreds of kilometers to the east and during the early and middle Miocene (from 23 to 11 My ago), was displaced westward, colliding with and deforming the external zone. During this drift of the internal zone, important east–west dextral strike-slip fault bands, situated in the Alpujarran Corridor, formed, cutting the zone and facilitating the westward displacement of its southern parts. Originally, the faults of the Alpujarran Corridor presented lateral displacements of dozens of kilometers, deeply cutting the crust. Later, from the beginning of the late Miocene (11 My ago), the Betic Cordillera underwent a geodynamic change and was subjected to approximately north–south compression. Owing to this new stress regime, lateral movement practically ceased, and important reliefs began to form, forming the great anticline of the Sierra Nevada (Fig. 2) or the progressive uplift of Sierras Almijara and Tejeda (Figs. 2, 3). Beginning at this time, the east–west faults of the Alpujarran Corridor began to move differently, with nearly vertical motion, along normal or reverse faults. Another domain worth mentioning in the Betic Cordillera is the Flysch units located in many places between and overlying the external and internal zones (Fig. 2).

The VZF (Fig. 3) in the Sub-betic zone presents well-preserved scarps dipping approximately 70° N, in which it is possible to observe vertical striae, sometimes with a dextral component (Galindo Zaldívar *et al.*, 2004; Sanz de Galdeano, 2013). This characteristic indicates that the fault is normal, with a dextral component, in the western part of the VZF. Eastward, in the internal zone, at an observed scarp, this fault is nearly vertical or dips at approximately 80° N and generally exhibits vertical striae. Moreover, at this fault, in both sectors, there are other parallel fault lines (Fig. 3). All of these faults can be considered part of the same fault band system (Sanz de Galdeano *et al.*, 2019). These faults surely coalesce at depth, forming a resulting important fault.

As indicated, beginning in the late Miocene 11 My ago (Sanz de Galdeano and Alfaro, 2004; Sanz de Galdeano, 2013), the relief of Sierras Tejeda and Almijara (Fig. 3) progressively increased, reaching values of 2000 m or even greater, at present not observable due to the effects of erosion. In contrast, in the northern block of the east–west-oriented faults in the southern part of the Granada basin (Arenas del Rey, Játar, and Jayena areas; Fig. 3), the heights are much lower, that is, on the order of 800–900 m, height that would be even lower

if that sector had not been filled by the important sedimentation of the material eroded in Sierras Tejeda and Almijar.

This height difference is the result of the accumulation of vertical displacements (throws) produced by many displacements along these faults. This process continues, as shown by Quaternary surfaces dipping to the south (glacis) in the southern part of the area of the Granada basin (Arenas del Rey-Játar sector); these surfaces originally sloped northward (Sanz de Galdeano, 1985). Finally, the throw of this fault band, which is greater than 1000 m, together with the lengths of these faults, leads us to surmise that they cut deeply into the crust. Therefore, the earthquakes that have occurred in this sector, of which the 1884 earthquake is the largest known, likely correspond to motions on normal faults oriented approximately east–west to west-northwest–east-southeast.

Seismicity and Focal Mechanisms

The 1884 earthquake occurred in a seismically active zone, that is, the plate boundary between Eurasia and Africa (Udías and Muñoz, 1979; Buforn *et al.*, 1988). The boundary is better defined in the oceanic part, west of 12° W. Near the Iberian Peninsula, in an oceanic to continental transition, the plate boundary forms a wider deformation zone, extending from southern Iberia to northern Africa (Buforn *et al.*, 2004). Figure 4 shows the distribution of large earthquakes for the period from 1500 to 2024, with a maximum intensity equal to or greater than VIII–IX (triangles) or a magnitude M_w equal to or greater than 6.0 (circles). In southern Spain, these earthquakes are located in an area extending east-northeast–west-southwest, corresponding to the Betic Zone (Fig. 2). Large historical earthquakes that have occurred from east-northeast to west-southwest include the 1748 Montesa (I_{max} = IX, Buforn *et al.*, 2015), 1829 Torrevieja (I_{max} = IX–X, Muñoz and Udías, 1991), Almeria 1522 (I_{max} = VIII–IX, Vidal, 1986), and 1804 (I_{max} = VIII–IX, Murphy Corella, 2020), 1680 Malaga (Goded *et al.*, 2008), and 1504 Carmona (Gentil and de Justo, 1983) earthquakes. Offshore, the epicenters are located on both sides of the Gibraltar Strait (GS). West of the GS, the large 1755 Lisbon (I_{max} = X) and the 1969 southwest Saint Vincent Cape (M_w 7.8) earthquakes both generated tsunamis (Martínez-Solares and López Arroyo, 2004; Buforn *et al.*, 2020). East of the GS, large earthquakes continued to propagate inland along the northern coast of Algeria, where the 1790 Oran de (I_{max} = IX–X, Buforn *et al.*, 2019) and 1980 El Asnam (M_w 7.1, Deschamps *et al.*, 1982) earthquakes occurred. In the Alboran Sea, east of the GS, there has been an increase in activity since the end of the twentieth century, with the occurrence of **M** > 6 earthquakes in 2004 (M_w 6.3, Stich *et al.*, 2005) and 2006 (M_w 6.4, Buforn *et al.*, 2017).

Recent earthquakes (2000–2023) of **M** ≥ 3.0 at the southern Iberian Peninsula and northern Africa have mainly shallow foci (h < 40 km, red circles in Fig. 5). In addition, earthquakes have occurred at intermediate depths (40 < h < 150 km, green circles in Fig. 5) located mainly offshore, and one earthquake has occurred at a very deep depth (h = 650 km, blue circles in Fig. 5). West of the GS, most earthquakes have been shallow in depth, with some intermediate-depth earthquakes following a similar alignment. East of the GS, most activity clusters along the northern African coast, corresponding to shallow earthquakes, where the M_w 6.2–6.4, 2004 Al-Hoceima and 2016 Alboran earthquakes occurred (Figs. 4, 5). Another characteristic of seismicity east of the GS is the occurrence of intermediate-depth earthquakes (green circles), predominantly extending north–south at 4°–5° W (Buforn *et al.*, 1997; López-Sánchez *et al.*, 2022), and very deep earthquakes (blue circles). The epicenter of the 1884 earthquake (black star in Fig. 5) is located at the northern end of the intermediate-depth earthquakes and ∼50 km east of the 2010 deep (h = 637 km) earthquake (Fig. 5, blue dot).

The seismicity in the epicentral area of the 1884 earthquake (rectangle in Fig. 5) for the 1980–2023 period with magnitudes of **M** ≥ 3.0 (see Data and Resources) was low, with a maximum magnitude of M_w 4.3. Most shallow earthquakes in the area occurred north of the 1884 earthquake and at intermediate depths to the south (Fig. S1).

Different authors have determined seven focal mechanisms in the 1884 epicentral region (1984–2024, **M** 4) by moment tensor inversion using observations at regional distances. All focal mechanisms located east of the 1884 earthquake epicenter have one plane with predominant near-vertical motion. Five solutions (events 1984, 1996, 1998, 2003, and 2009) have normal-faulting mechanisms with nearly vertical planes oriented northwest–southeast to north-northwest–south-southeast (Fig. S2, Table S1). The stress regime corresponds to horizontal northeast–southwest to north–south extension or dips of 45° to the northeast (event 1997). One exception is the 2014 earthquake, with reverse faulting and horizontal pressure axes in the north-northeast–south-southwest direction, but this occurred at intermediate depths (60 km), whereas the others were all shallow.

Reevaluation of Seismic Intensities

We have undertaken archival research to find additional accounts about reported damages produced by the 1884 earthquake, with new information from national and local newspapers that provides information never previously used. The period that was evaluated extends from 25 December 1884 (the date of the earthquake) to 8 January 1885 for daily newspapers and to 11 January 1885 for other publications. We have considered only information from primary sources. Table S2 gives a list of consulted newspapers.

We have examined the existing evaluations of intensities and added new evaluations on the basis of contemporary descriptions of the damage produced by the earthquake in different towns and villages. We have accepted the intensity values given by Martínez-Solares and Mezcua (2002), who assigned intensity values using the EMS-98, with the following modifications.

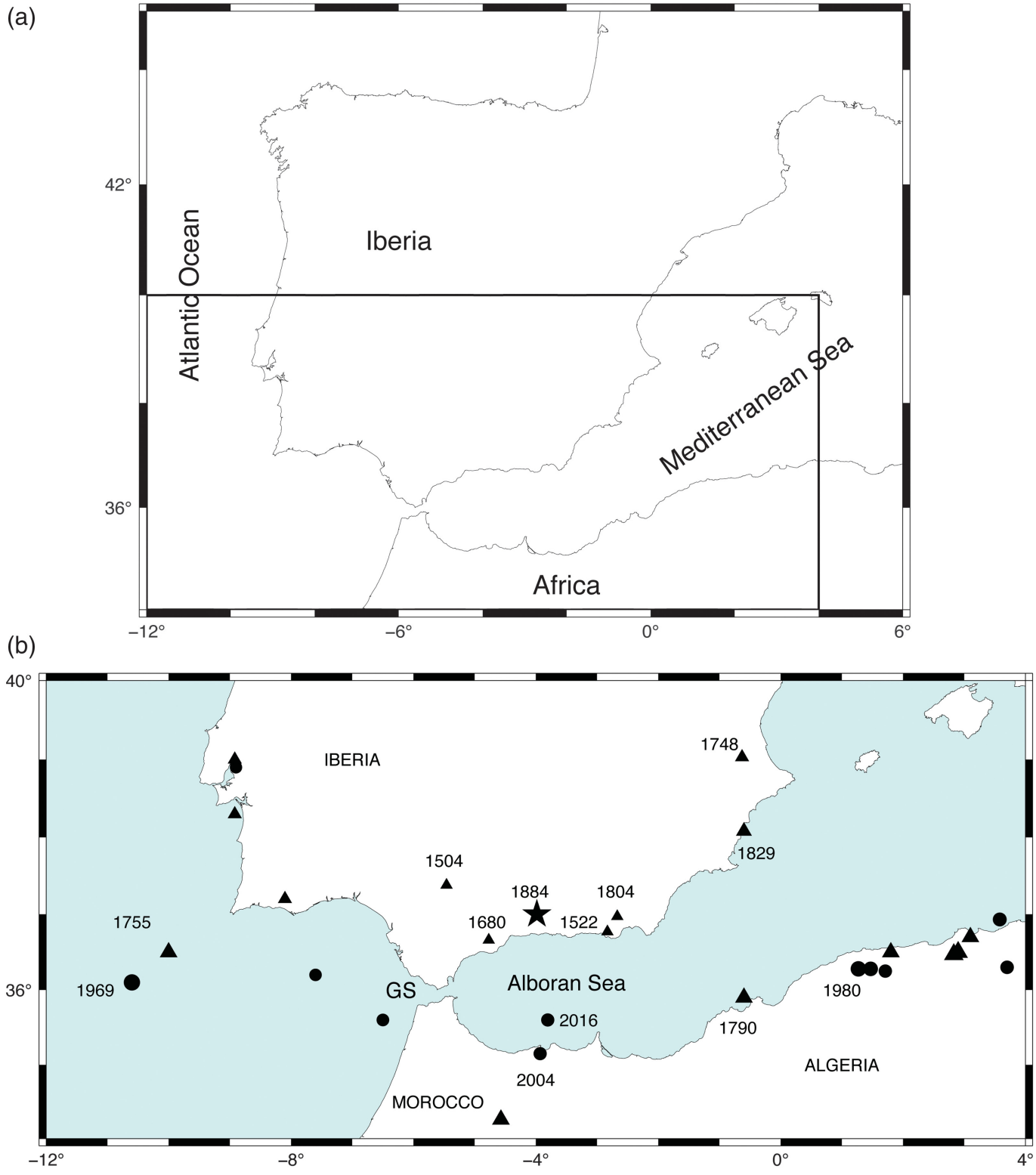

1. We have added new values that were not included in Martínez-Solares and Mezcua (2002), for locations for which new information has been found (bold type in Table S3).
2. We have re-evaluated the intensities that were included in Martínez-Solares and Mezcua (2002) for locations for which new information has been found (marked with an asterisk in Table S3).

Figure 4. (a) Location of the studied region. (b) Larger earthquakes occurred from 1500 to 2020 in southern Spain and surrounding regions. The triangles correspond to historical earthquakes with $I_{max} \geq$ IX (1500–1900), and the circles correspond to earthquakes (1960–2020) with **M** ≥ 6.0. The star shows the epicenter of the 1884 earthquake (see Data and Resources). GS, Gibraltar Strait.

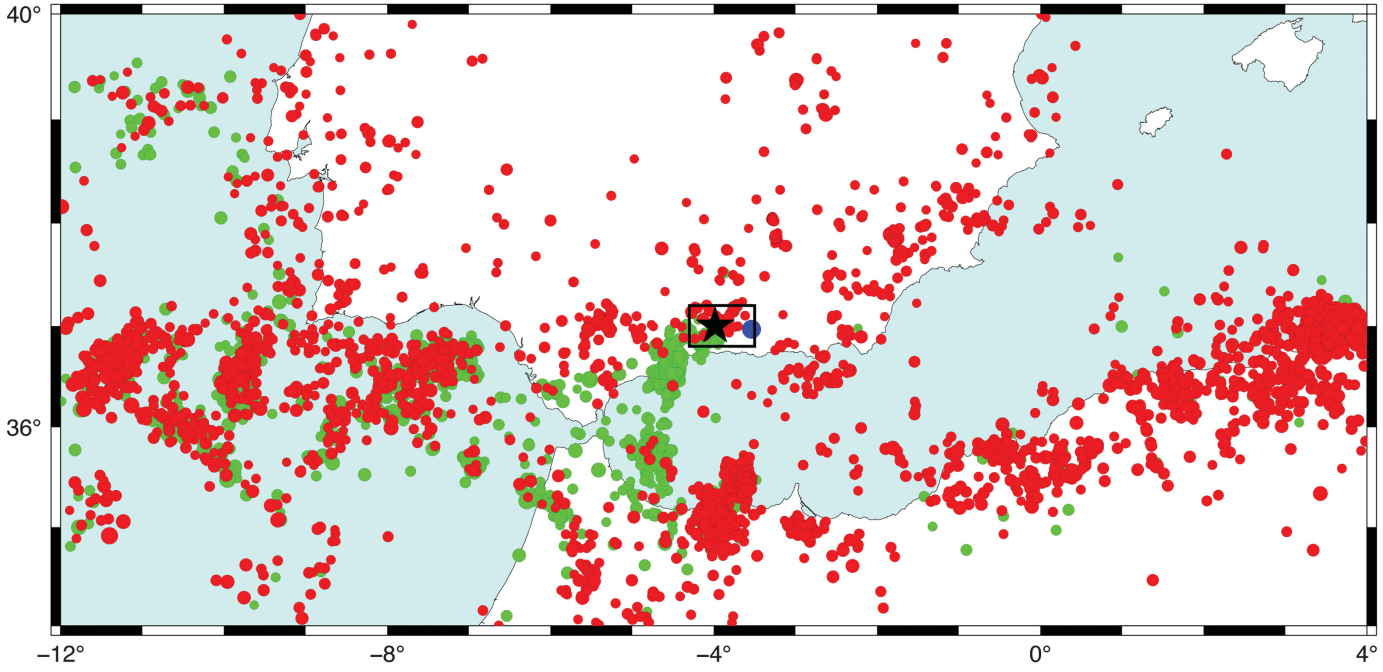

Figure 5. Seismicity for the 2000–2024 period (**M** ≥ 3.0) in southern Spain and surrounding regions taken from the Instituto Geográfico Nacional (IGN) catalog (see Data and Resources). Red circles correspond to shallow earthquakes (h < 40 km), green circles correspond to intermediate-depth earthquakes (40 < h < 150 km), and blue circle corresponds to deep earthquake (h > 600 km). Star is as in Figure 4. GS, Gibraltar strait.

We have accepted the re-evaluation of Martínez-Solares and Mezcua (2002) for the locations with the greatest damage (intensities VIII–X), for which no new information has been found. Fernández de Castro *et al.* (1885), Orueta y Duarte (1885), Taramelli and Mercalli (1885), Fouqué (1889b), López-Arroyo *et al.* (1981), and Vidal (1986) have given a detailed description of the damage. We summarize it here for the largest and no modified intensities using the EMS-98, where damage grade, 1–5, and vulnerability class A–F are specified. Most houses affected by the earthquake were of a simple stone masonry structure, vulnerability A–B. A short summary follows of the villages with the highest assigned intensities IX–X and IX.

Arenas del Rey (1356 inhabitants) is the village with the maximum intensity IX–X. It was destroyed, 90% of buildings had damage of grade 5 (total or near total collapse), and the rest had damage of grade 4 (serious failure of walls; partial structural failure of roofs and floors).

Sites with assigned intensity IX are as follows. In Alhama de Granada (7758 inhabitants), 70% of houses had damage grade 5, 15% damage grade 4, and the rest damage grade 2–3 (cracks in many walls, partial collapse of chimney—large and extensive cracks in most walls, failure of individual nonstructural elements). In Figure 1, we show an example of damage in this town. In Periana (4060 inhabitants), 57% of houses had damage grade 5, and the rest had damage grade 4. In Zafarraya (2700 inhabitants), 38% of buildings had a damage grade 5, the church was destroyed, and 32% with damage grade 3–4. In Alcaucín (2019 inhabitants), 20% of houses were destroyed and 80% with severe damage. In Jayena (1213 inhabitants), 60% houses and the church with damage grade 5, the rest with damage grades 4 and 3. In Jatar (1163 inhabitants), 30% of the houses were damaged to grade 5, 40% to grade 4, and the rest to grades 2 and 3. In Albuñuelas (1640 inhabitants), 58% of houses had damage grade 5 and 3% damage grade 4. In Ventas de Zafarraya, a village with 934 inhabitants, 60% of the houses suffered grade 5 damage and the rest grade 4, and some cracks in the ground. In Fornes, Cacín, and Santa Cruz del Comercio (746, 728, and 708 inhabitants, respectively), 60%–70% of houses with damage grades 5 and 4, and the rest with damage grades 2–3.

The number of casualties varies according to sources, with an estimated total of 839 (López-Arroyo *et al.*, 1981), but all of them agree that the highest number corresponds to Alhama de Granada, more than 300. Arenas del Rey 135 and Ventas de Zafarraya 70. In other villages such as Alcaucín, Cacín, or Jatar and the reported casualties are less than 6.

Considering the reported damage, we have assigned intensity VIII to Algarrobo, Archez, Arenas, Canillas de Aceituno, Canillas de Albaida, Competa, Frigiliana, Melegís, Murchas, Restabal (El Valle), Salares, Saleres, Sayalonga, Sedella, Torrox, Vélez-Málaga, and Viñuela. In these villages, 25%–50% of houses had damage grade 5 or 4. For example, in Canillas de Aceituno, 15% of the buildings collapsed and 65% of the houses suffered damages of grades 3 and 4. In Canillas de Aceituno and Vélez-Málaga there were 5 and 6 fatalities, respectively.

We have assigned an intensity of VII–VIII to the locations with the greatest damage for which we have found new

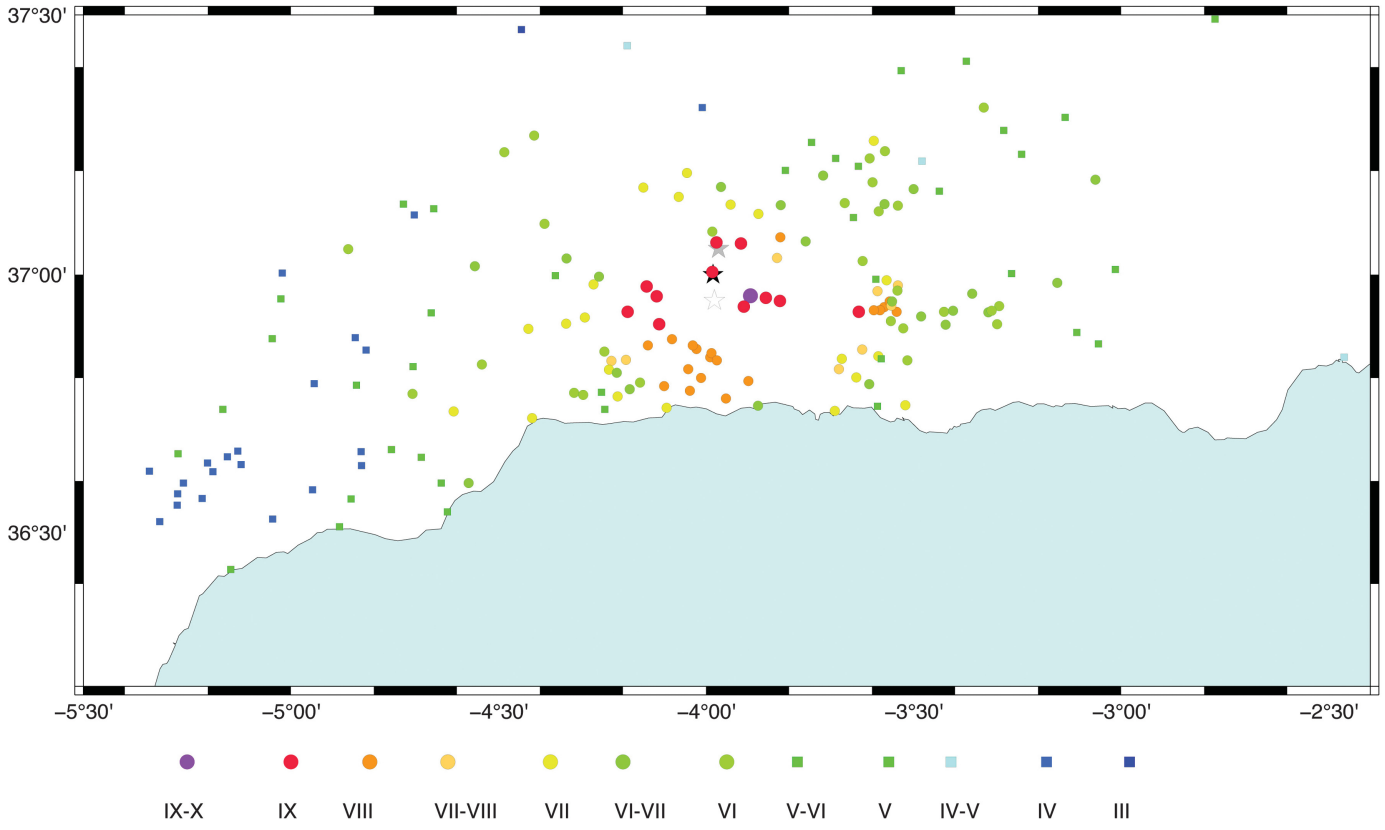

Figure 6. Re-evaluation of intensities (European Macroseismic Scale 1998 [EMS-98]) for the 1884 earthquake. Stars show the 1884 epicenter: black represents the IGN epicenter, white represents the Udías and Muñoz (1979) epicenter, and gray represents the Mezcua *et al.* (2020) epicenter.

information which corresponds to the village of Conchar. The rest of the new information we have found corresponds on damage to locations with low intensities (lower than VII, Table S3).

A description of the damage corresponding to the locations with new or re-evaluated intensities is given in the supplemental material; here, we summarize this information. First, the damage information refers to all cases of small villages, with buildings mostly belonging to vulnerability class A. We assigned the largest revised intensity value, VII–VIII (EMS-98), to Conchar, which is a small village where 9 of the 10 houses were near collapse or ruin (Table S3). We assigned intensity VII to the village El Turro, where only four of the 80 existing houses were made inhabitable, and the church was destroyed. We assigned intensity VI–VII to locations where there was ruin in some houses and damage (cracked walls) to others, with a partial collapse of the church. We assigned intensity VI to locations where some houses were ruined but others remained undamaged, and where there was partial damage to the churches or the bell towers. At some sites, some buildings (houses, churches, and bell towers) had cracks and were assigned intensity V–VI. We assigned intensity V to sites where there was some damage to houses and where the earthquake was experienced by the population. We finally assigned "D" to locations where damage was reported but no details about the damage were recorded, "F" when the earthquake was felt, and "GE" to ground effects, such as sinks or cracks.

Figures 6, 7, and Figure S3 show the new map of intensities: the highest intensity, I_{max} = IX–X (EMS-98), corresponds to the village of Arenas del Rey, where the reported damage was the greatest. IDPs with an intensity of IX (Figs. 6, 7, red circles) correspond to the villages of Albuñuelas, Alcaucín, Alhama de Granada, Cacín, Fornes, Játar, Jayena, Periana, Santa Cruz del Comercio, Ventas de Zafarraya, and Zafarraya (Fig. S3) within an area elongated in the east-west direction. IDPs with an intensity of VIII (orange circles) are grouped into two zones: one south-southwest of the epicenter (Algarrobo, Archez, Arenas, Canillas de Aceituno, Canillas de Albaida, Competa, Frigiliana, Salares, Sayalonga, Sedella, Torrox, Vélez-Málaga, and Viñuela) and one east of the epicenter (Melegís, Murchas, Restabal [El Valle], and Saleres). A third zone of intensity VIII corresponds to Ventas de Huelma, which is northeast of the epicenter. The distribution of weaker intensities, that is, VII–V (green circles and squares), is very homogeneous but again is east–west elongated. Finally, importantly, there are no IDPs with values less than V to the east, but in contrast, several are reported to the west. This may be due to the different distributions of villages on both sides. The

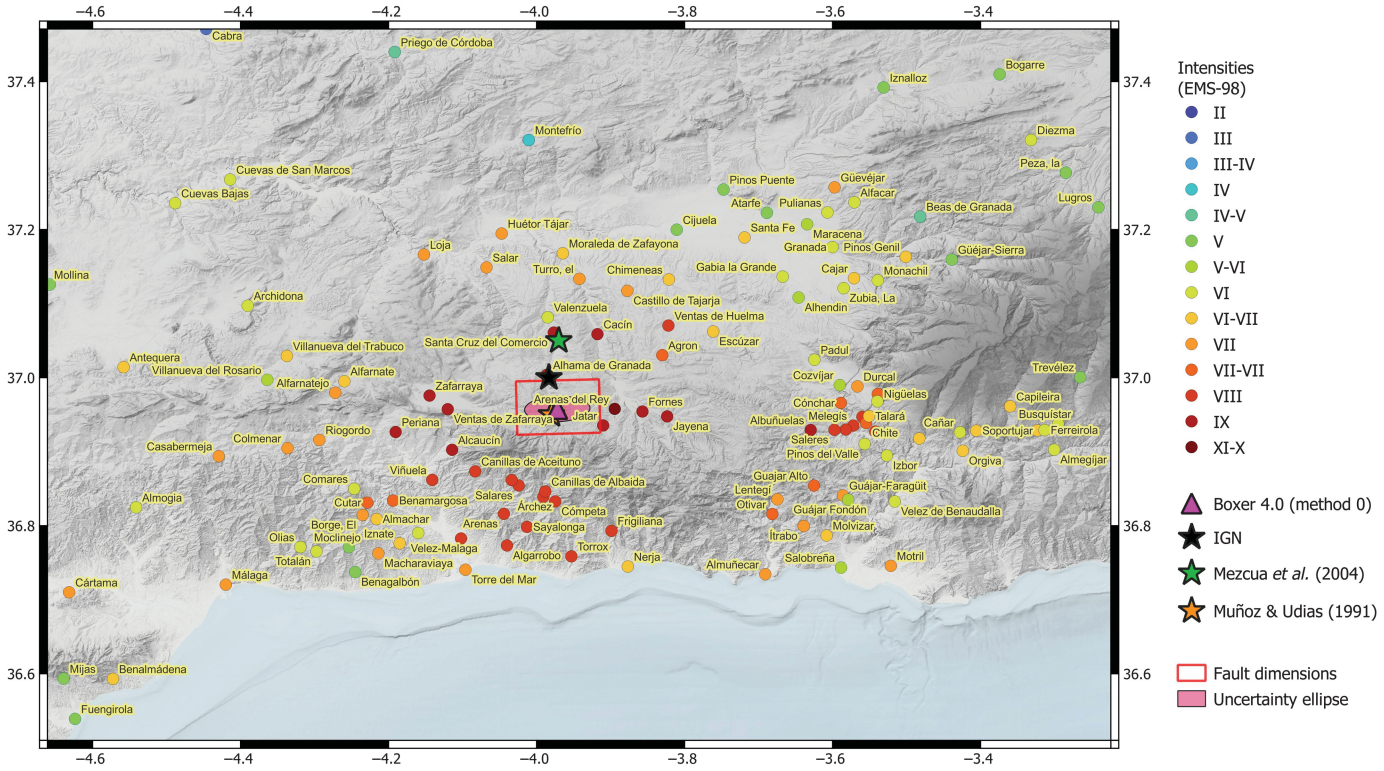

Figure 7. Intensities of the epicentral area and macroseismic epicenters. Black star denotes Martínez-Solares and Mezcua (2002), orange star denotes Udías and Muñoz (1979), green star denotes Mezcua *et al.* (2004) epicenters, pink triangle denotes macroseismic epicenter estimated in this article using Boxer 4.0, and pink ellipsoid denotes uncertainties.

resulting intensity map is not very different from those of Udías and Muñoz (1979) and Martínez-Solares and Mezcua (2002) but provides greater detail. The main difference is the increase in the number of intensities VI–V, and V to the east, which agrees with the isoseismal map of Vidal (1986); however, this map has lower IDP values to the west. The epicentral zone, which experienced the greatest damage ($I_{max} \geq$ IX), has an area of ~66 km × ~22 km. Taramelli and Mercalli (1885) already identified the zone of greatest damage (*disastroso*) as an elongated east–west area but with a smaller extent (less than 13 km in length by 4 km wide). In our map, the total area with intensities greater than VI corresponds to a region of ~140 × 50 km^2.

We have obtained a relationship between intensity (blue circles) and distance using an equation similar to that proposed by Martín (1984) for this region (red curve in Fig. S4):

$$I = 17.76 - 2.96 \times \log(R + 15) + 0.0087 \times (R + 15), \quad (1)$$

in which I is the intensity and R is the epicentral distance in kilometers.

We used the BOXER 4.0 method 0 (Gasperini *et al.*, 1999, 2010) to estimate the epicenter location, which corresponds to the barycenter of the damaged area because the event occurred with an inland focus, with a usable number of IDPs and good azimuthal coverage. This epicenter is very close to that obtained by Udías and Muñoz (1979) and is also based on the distribution of the highest intensity values with small uncertainties (5 and 2 km for the semimajor and minor axes of the bootstrap uncertainty ellipse (Table S4 and Fig. S5).

This method estimates an equivalent moment magnitude equal to 6.0 ± 0.1, which depends on the magnitude–intensity (M-I) relationship used (Vannucci *et al.*, 2021; Vannucci, 2024). In our study, we have used an M-I relationship specific for the Betics region (Mezcua *et al.*, 2020, 2013). However, the magnitude obtained with BOXER 4.0 method 0 is underestimated (6.0) versus previous estimated magnitudes of 6.8–7.0 (Udías and Muñoz, 1979) and 6.5 (Martínez-Solares and Mezcua, 2002). It is important to note that BOXER is a model that works with the available data. In Figure S4, we can observe that the M-I relationship proposed by Mezcua *et al.* (2020) overestimates the intensity values. For example, for a distance of 100 km and magnitudes of 6.5 and, results in intensities VI and VII, respectively, when the mean observed is an intensity of V. To obtain magnitude in the range of 6.5–7.0, we need higher epicentral intensities (X to X–XI) not observed in our case. Vannucci *et al.* (2021) and Vannucci (2024) show that in Italy, magnitudes for the early 1900s earthquakes can be overestimated by 0.1–0.2 units, whereas the M-I relationship for the Betics (Mezcua *et al.*, 2020) underestimates the magnitude by up to 0.6–0.8 units.

BOXER also calculates a possible seismogenic area. This model corresponds to a rectangular fault oriented in the

east–west direction, which is in agreement with the VZF and has dimensions of 12 km × 8 km (Fig. 7). The Rayleigh and Kuiper tests both are <0,1 (Table S4), so we prefer to discard these values. These magnitudes and dimensions are lower than those obtained by Udías and Muñoz (1979) (**M** 6.7–7.0 and lengths of 20–30 km). The Udías and Muñoz (1979) and BOXER epicenter may be affected by the highest intensity (IX–X) observed only in Arenas del Rey village, which was located approximately 800 m southwest of the present site where the village was rebuilt after the earthquake. The town was first located in a flat area bordering the side of a mountain, formed by little compacted material. This type of terrain may have amplified the ground motion and could explain the high damage.

Distribution of Ground Acceleration and the Source Model

As already mentioned, the 1884 earthquake was associated with a rupture on the VZF based on geological, paleoseismic, and, more recently, Global Navigation Satellite Systems evidence. However, all contemporary surveys conducted after the earthquake revealed that there was no observable fault rupture on the surface of the VZF; rather, only cracks, landslides, and ground subsidence over a large area. Thus, the only direct seismological observations for this earthquake are the observed intensities. We propose here a model for the source of the earthquake based precisely on these observations.

To determine the source model, we begin using an approximation of the PGA values derived from the observed intensities, although it must be taken into account that the conversion between intensity and PGA is less straightforward than it seems (Gallahue and Abrahamson, 2023). Because there are no specific empirical relationships between intensity and PGA for Spain, we tested several relationships (Murphy and O'Brien, 1977) that have been used in similar studies for Spain (Buforn *et al.*, 2015) or Italy (Faenza and Michelini, 2010; Masi *et al.*, 2020; Oliveti *et al.*, 2022). The theoretical PGA values obtained from these relationships are compared with the few observations of Spanish earthquakes, such as those for the 2011 Lorca earthquake (M_w 5.1, I_{max} = VII, PGA = 3.53 ms^{-2}) and the seismic series of the 2021 Granada earthquake (M_w 4.4, I_{max} = V–VI, PGA = 1.61 ms^{-2}). The relationship by Oliveti *et al.* (2022) (following equation), which gives the PGA values with margins of error, is the relationship that gave the best results:

$$I = 3.01 \pm 0.12 + 0.86 \pm 0.04 \log^2 \mathrm{PGA}, \quad (2)$$

in which I is the EMS-98 intensity and the PGA values are in square centimeters. From this relationship, we obtained PGA values that correspond to the observed IDP values; for example, for I_{max} = IX–X, the acceleration is 5.59 ms^{-2}. This spatial distribution of PGAs was used as the "observed values" to investigate the source parameters proposed for the 1884 earthquake.

The spatial distributions of PGVs and PGAs were strongly affected by the location, magnitude, and focal mechanism of the earthquake (Vidale, 1989; Ma *et al.*, 2019), as well as by rupture directivity (Cultrera *et al.*, 2009; Seekins and Boatwright, 2010; Xie *et al.*, 2017; Hough and Graves, 2020). In addition, in the case of large earthquakes, finite source properties, including the size and geometry of the rupture and the presence of earthquake directivity, can modulate the PGA pattern. Finally, the observed PGAs may be affected by local, structural heterogeneities controlling attenuation and site effects that are not known.

Several recent studies have used the spatial distribution of PGAs to constrain earthquake source parameters (Hough *et al.*, 2005, 2022; Griffin *et al.*, 2019; Hough and Graves, 2020; Martin and Hough, 2022; Gallahue and Abrahamson, 2023). A stochastic finite source modeling approach, accounting for the source, path and site effects, was successfully applied to strong-motion data from the 2017 M_s 7.0 Jiuzhaigou earthquake in China (Sun *et al.*, 2018) to resolve its slip distribution. Buforn *et al.* (2015) modeled PGAs for a constrained focal mechanism to resolve the depth, magnitude, and rupture plane orientation for the 1748 Montesa earthquake in Spain.

In our simplified modeling, we use rectangular fault models with uniform slip and different rupture directivities but neglect further source complexities, such as the presence of asperities, complex source time functions, or rupture plane bending, and we assume a uniform 1D velocity model, negating local path and site effects. Under these conditions, it may be challenging to reproduce absolute PGAs (the M1 approach), but the spatial distribution of relative PGAs (i.e., using normalized values) can still be used to constrain some source parameters (the M2 approach). Consequently, we also choose to fit the normalized PGA values using a cosine norm. The absolute PGA values are fitted using an L2 norm.

The proposed simulations for the earthquake rupture models allow the estimation of absolute and normalized PGAs that can be compared with those derived from the observed intensity values. For this purpose, we compute synthetic acceleration records, assuming rectangular source models with different geometries and homogeneous slip distributions. We use *Pyrocko* tools (Heimann *et al.*, 2017) to simulate the rupture of a finite source. We discretize it into a spatially homogeneous distribution of point sources, which are activated at the time the rupture front reaches them. We obtained synthetic seismograms for each point source by convolution of the point-source moment tensor with Green's functions, which are computed for a regional velocity model (Bassin *et al.*, 2000). Specifically, we tested 181,440 models, sampling a realistic range of rupture sizes, source depths, fault-plane orientations, dimensions, and fault motions. For the fault planes, the strike (from 0° to 360°), dip (from 0° to 90°), and rake (from −180° to 180°) vary at intervals of 15° for each variable. Given the usage of PGA values only (we do not have any waveforms), there is no possibility of distinguishing between

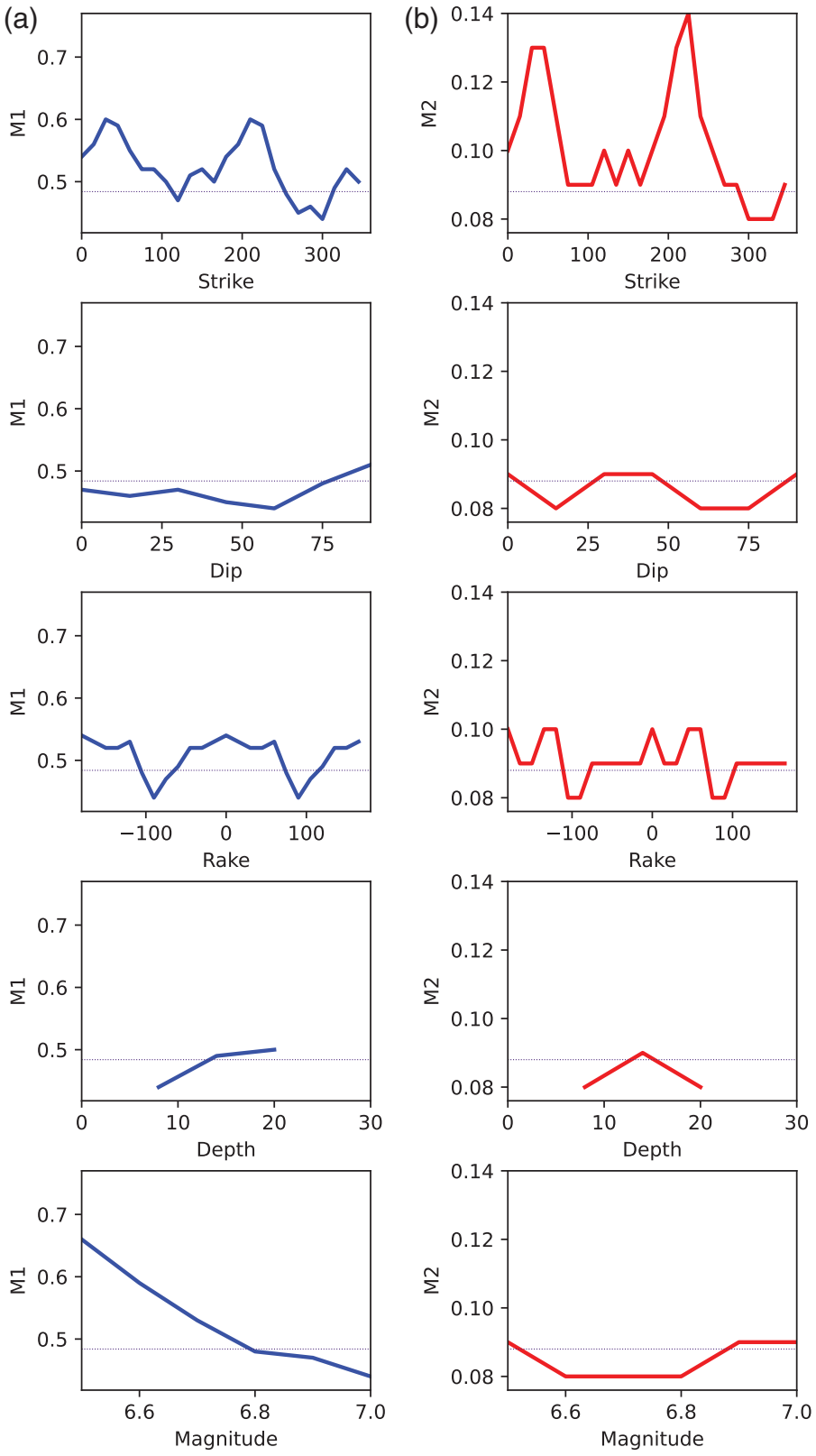

Figure 8. Misfits for the strike, dip, rake, depth, and magnitude. (a) Absolute peak ground acceleration (PGA) values and (b) normalized PGA values.

reverse and normal focal mechanisms (with common strike and dip and positive or negative rake values). We also tested three possible focal depths, 8, 14, and 20 km, and seismic moments corresponding to M_w values ranging from 6.5 to 7.0, with an interval of 0.1. The proposed source model corresponds to a rectangular fault with uniform slip. For the fault dimensions (length and width), the lengths range from 24 to 49 km, and the widths range from 11 to 17 km, according to empirical relations (Wells and Coppersmith, 1994). We further reduce the width whenever the rupture reaches the surface, according to the lack of surface rupture observations. Furthermore, we tested five different kinematic models: rupturing outward (bilateral rupture) and unilateral ruptures in four directions (up-dip, down-dip, along strike, and against strike).

The two misfits (approach M1 and approach M2) between the synthetic and "observed" PGA values as a function of the five estimated source parameters (strike, dip, rake, depth, and magnitude) produce similar results, except for the magnitude (Fig. 8). With respect to the fault plane orientation, we prefer a strike range of 270°–330° for both misfits; a strike of ~300° (west-northwest–east-southeast) is the most likely strike, considering both results and rakes of ±75°–105°, corresponding to a predominant normal (the northern part exhibiting downward motion and the southern part exhibiting upward motion) or thrust mechanism (opposite motion). The dip is toward the north, but the angle is poorly resolved,

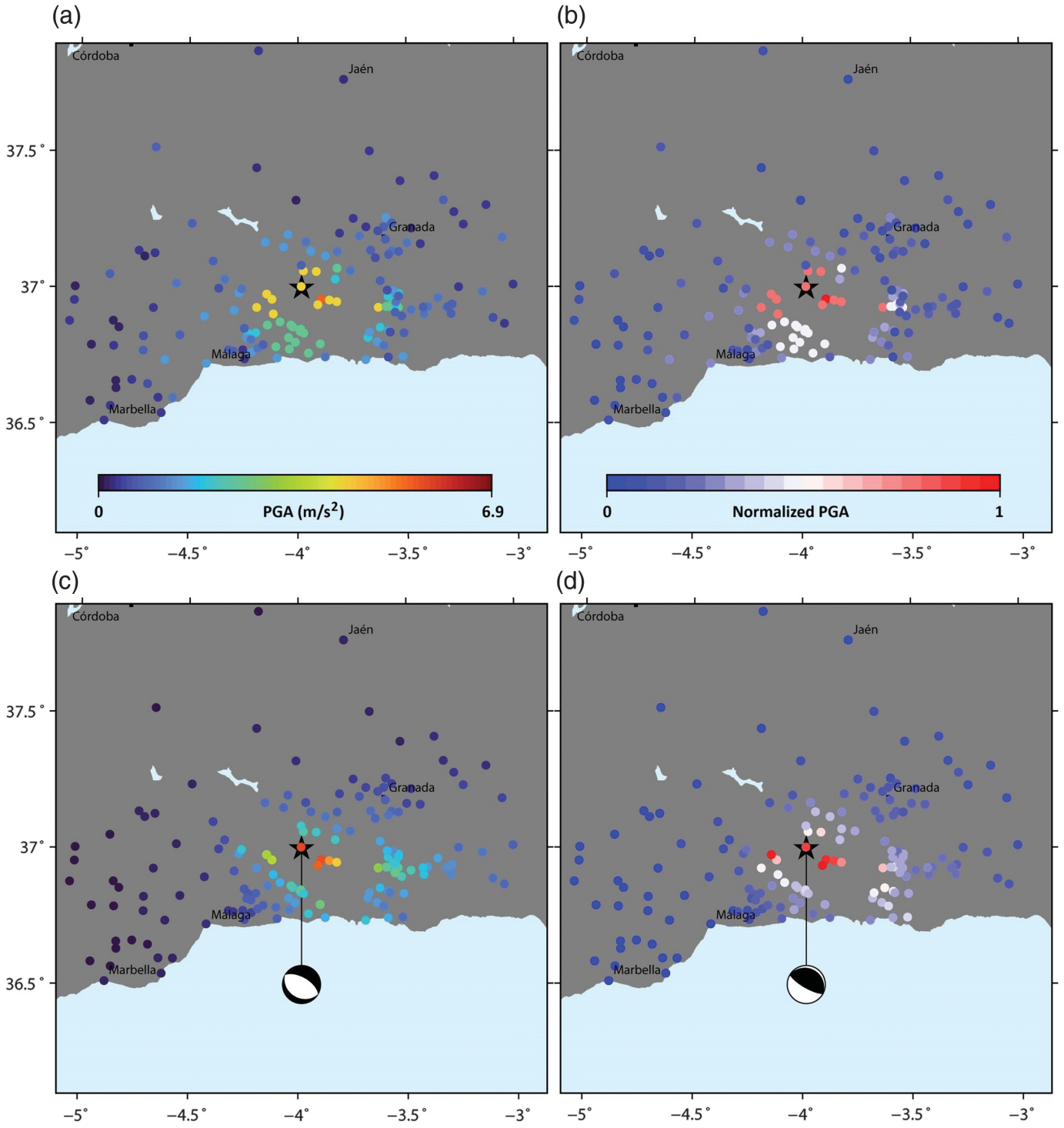

Figure 9. Distribution of PGA values. (a) Absolute values are derived from intensities, (b) normalized values are the same as in panel (a), (c) synthetic absolute PGA values are for the plotted focal mechanism, and (d) normalized PGA values are the same as in panel (c). Stars correspond to the IGN epicenter.

with possible solutions, showing either a steep or low dip angle. A shallow depth (here, 8 km) is preferred for both misfits, but the M2 approach has a poorer resolution. The magnitude has a poor resolution, with discrepant results.

Figure 9 shows the "observed" PGA values derived from intensities and predicted by synthetics using the first approach (M1, Fig. 9a,c) or the second approach (M2, Fig. 9b,d). Both approaches produce similar results in terms of the focal mechanism and depth. Some focal mechanism parameters are quite robustly resolved. The fault plane appears to be oriented roughly east–west to west-northwest–east-southeast, dipping north to north-northeast. We show an example of the distribution of the synthetic PGA for approach M1 (Fig. 9c) for the fault-plane orientation, with a strike of 300°, dip of 60°, and rake of −90°, and

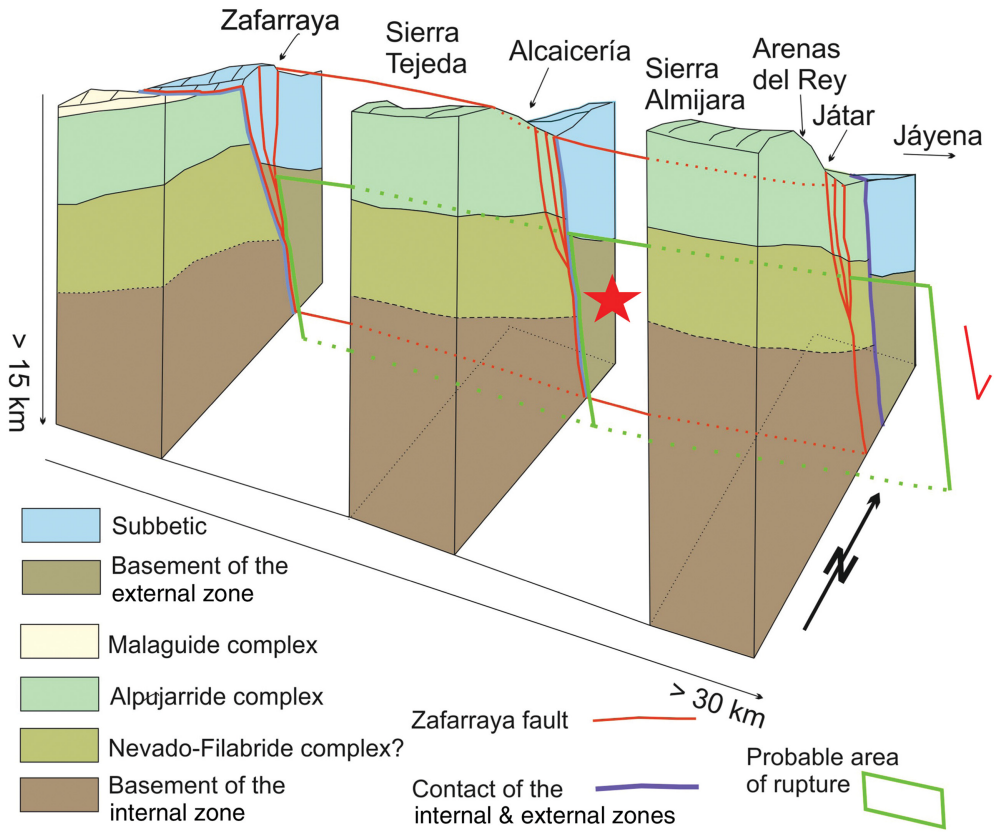

Figure 10. Schematic diagram showing the epicentral area of the 1884 earthquake. The red star shows the hypocenter of the 1884 earthquake.

for M2 (Fig. 9d), with a strike of 330°, dip of 15°, rake of 75°, depth of 8 km, and M_w 6.7. This orientation is constrained by the west-northwest–east-northeast band of higher PGAs (Fig. 9c,d). The rake angle is also well resolved (Fig. 8), suggesting either predominant thrust faulting or normal faulting, with only minor oblique components. In general, we prefer a shallow crustal source because of the poor resolution of its magnitude, which is controlled only by high PGA values. This fault orientation agrees with the orientation obtained through the BOXER code, showing that it is a reliable methodology to establish the faults responsible for an earthquake using macroseismic data (Vannucci *et al.*, 2019).

Discussion

In this work, we propose a source model for the 1884 earthquake that can reproduce the spatial distribution of PGAs derived from intensity values. The source model has a rectangular rupture area striking east–west to west-northwest–east-southeast direction (strikes of 270°–330°) and nearly vertically dipping, with lengths of 28–40 km, widths of 11–14 km, and average slips of 0.6–1.0 m. For the rake angle, the polarity of the focal mechanism remains unresolved when PGA values are used only: the mechanism type can either correspond to dominant thrust faulting or normal faulting, with rakes in the range of 75°–105°, or −105° to −75°. However, only a normal-faulting rupture type is consistent with VZF fault motion and regional geological setting. The focal depth is well defined at 8 km, which agrees with the intensity distribution. The corresponding estimated scalar seismic moment M_0 ranges from 0.8 to 2.0×10^{19} N · m, with corresponding M_w magnitudes of 6.6–6.8; however, these values should not be taken as definitive because they may be underestimated or overestimated. According to this model, the rupture would not reach the free surface, which is in agreement with contemporary reports of the absence of an observable surface rupture on the VFZ (Fig. 10).

This source model accords with the opinions of most authors who have studied the 1884 earthquake and attributed it to the VZF system (Sanz de Galdeano, 1985; Reicherter *et al.*, 2003; Rodríguez-Peces *et al.*, 2011; Grützner, *et al.*, 2013; Mudarra-Hernández *et al.*, 2023; Madarieta-Txurruka *et al.*, 2024). A relatively large variation in the strike (270°–330°), which partially reflects the intrinsic uncertainties of a source inversion based on PGAs only, also manifests the complexity of the region's geology. Indeed, the VZF system shows significant changes in azimuth: from east-northeast–west-southwest in Periana in the west to a variety of directions from west-northwest–east-southeast to east-northeast–west-southwest in Zafarraya and further east to almost east–west in Játar and Jayena (Fig. 3). The VZF system itself is oblique to the contact between the internal and external zones; thus, eastward, the VZF system is in the internal zone, and westward, the VZF system crosses into the external zone (Fig. 10).

Another manifestation of this complexity is the intensity distribution. The zone of greater intensity (IX) extends in the east–west direction from Periana to Jayena (approximately 30 km, Fig. 3, Fig. S3), in accordance with the trace of the VZF. The maximum intensities (IX–X) are at the former location of Arenas del Rey, which is 1 km from the present location (the village was newly built after its destruction) of the VZF and could be explained by possible site effects. However, at Játar, which is very close to Arenas del Rey, the damage was not as large (IX) because of low-site effects in more consolidated

ground. Westward, near Periana and Guaro, the presence of less consolidated geological formations, such as the Flysch units (Fig. 3), resulted in increased landslides, land subsidence, and other ground effects. Site effects were very important in this zone because of the influence of the ground relief of the Sierra de Alhama to the north. A large ground crack was observed from Zafarraya to Játar, along Sierra Tejada, with a length of approximately 8 km (López-Arroyo *et al.*, 1981). However, these authors concluded that no observed ground rupture could be directly attributed to the earthquake. Finally, notably, in the zone of the Sierra de Alhama (south of Ventas de Zafarraya), previous earthquakes also produced notable ground deformations (Clavero *et al.*, 2024).

Our modeling approach involves different approximations concerning the estimation of PGAs. First, their derivation from intensities is based only on empirical relations for Italian earthquakes. Next, their forward modeling uses synthetic seismograms, which assume simplified source and 1D earth velocity models, neglecting local site effects. The lack of information in the epicentral zone, such as local site amplifications, may enhance a bias in the assignment of intensities and thus in the synthetic PGAs values. These approximations reduce the accuracy of absolute PGA estimation. However, comparable results obtained by fitting absolute or relative PGAs suggest that some source parameters (strike, rake, or depth) are robust, allowing an inference of the fault-plane orientation and thus identification of the causative fault. Our results confirm that the absence of analog or digital seismological recordings in historical earthquakes can be substituted with intensities. This approach may allow inference of the source parameters of historical earthquakes beyond estimates of the location or magnitude. The success of such studies depends on the availability of large intensity datasets with good spatial coverage, such as those used in this study. From a technical viewpoint, the proposed methodological approach, involving the independent inversion of source parameters using different norms, is suitable for assessing the robustness of results for future similar studies.

Conclusions

In this work, we have modeled the seismic source of the 1884 Andalusian earthquake on the basis of newly found contemporary damage information, which has increased the density and distribution of the observed intensities. Our approach highlights the possibility of studying the seismic sources of other historical earthquakes.

The estimation of PGAs, derived from intensities and their subsequent modeling, allows for the testing and comparison of different rupture models and the identification of those models that can explain the spatial pattern of peak accelerations. The methodology used for the modeling of PGAs independently uses two different norms that converge to the same model, strengthening the validity of our results.

For the 1884 earthquake, no surface rupture on the VZF was observed by contemporary analyses, contrary to what was reported by Reicherter *et al.* (2003). For this reason, we used a model of a rupture that did not reach the surface.

The proposed source fault model accords with the characteristics of the VZF system of faults, with an almost vertical plane dipping to the north and normal fault motion, with the northern part going down to contribute to the formation of the Granada basin and the southern part going up to form the Sierras Tejeda and Almijara. The strike of the obtained fault model (270°–330°) is well justified by the distribution of intensities in the east–west direction, with a larger extension west of the epicenter. This may indicate the possible effects of rupture directivity. The proposed focal mechanism of normal faulting also agrees with the focal mechanism found for small earthquakes in nearby areas.

The source parameters uncertainties reflect the limitations of the observations that were used (IDP distribution) and the geological complexity of the region. VZF is not a well-defined fault but rather an ensemble of normal faults oriented approximately east–west to west-northwest–east-southeast. This complex geology can explain ground-motion amplification due to site and ground effects, such as landslides, subsidence, and cracks produced by the earthquake. Our approach highlights the possibility of studying the seismic sources of historical earthquakes from the distribution of observed intensities.

Data and Resources

Software: *Generic Mapping Tools* (GMT, https://www.generic-mapping-tools.org/, last accessed March 2025), *Pyrocko* (https://pyrocko.org) information about damaged buildings is available online at the Instituto Geográfico Nacional (IGN, https://www.ign.es/web/ign/portal/terremotos-importantes, last accessed May 2024). Historical and instrumental seismic data can be found in the IGN online catalog (https://www.ign.es/web/ign/portal/sis-area-sismicidad, last accessed July 2024). A collection of photographs showing earthquake damage to buildings and ground effects is available at https://www.ign.es/web/resources/sismologia/publicaciones/Andalucia1884.pdf, last accessed February 2025). The anonymous gravure can be found online in the University of Berkeley (http://www.nisee.berkeley.edu/kozak/index.html, last accessed November 2024). Not re-evaluated intensities are available in Martínez-Solares and Mezcua (2002). Contemporary newspaper articles are available at https://hemerotecadigital.bne.es/hd/es/advanced, https://prensahistorica.mcu.es/es/inicio/inicio.do, https://www.bibliotecasdeandalucia.es/web/biblioteca-virtual-de-andalucia/inicio (all three websites last accessed February 2024). The supplemental material includes Figures S1–S5 and Tables S1–S4 (Table S3 includes a detailed description of damages for the new or re-evaluated intensity data point [IPDs]).

Declaration of Competing Interests

The authors acknowledge that there are no conflicts of interest recorded.

Acknowledgments

This work has been partially supported by the Spanish Ministry of Economy and Competitiveness (Project Number PID2021-122662OB-I00).

References

Bakun, W. H., and C. M. Wentworth (1997). Estimating earthquake location and magnitude from seismic intensity data, *Bull. Seismol. Soc. Am.* **87,** 1502–1521.

Bassin, C., G. Laske, and G. Masters (2000). The current limits of resolution for surface wave tomography in North America, *Eos Trans. AGU* **81,** F897.

Bilham, R., and S. E. Hough (2023). The 1886 Charleston, South Carolina, earthquake: Relic railroad offset reveals rupture, *Seism. Record* **3,** 278–288, doi: 10.1785/0320230022.

Buforn, E., M. Bezzeghoud, A. Udías, and C. Pro (2004). Seismic sources on the Iberia-African plate boundary and their tectonic implications, *Pure Appl. Geophys.* **161,** 623–646.

Buforn, E., P. Coca, M. Bezzeghoud, A. Udías, Y. Bouhadad, and M. Mattesini (2019). The destructive 1790 Oran (NW Algeria) earthquake in a region of low seismicity, *Tectonophysics* **759,** 1–14, doi: 10.1016/j.tecto.2019.03.008.

Buforn, E., P. Coca, A. Udías, and C. Lasa (1997). Source mechanism of intermediate and deep earthquakes in southern Spain, *J. Seismol.* **1,** no. 2, 113–130, doi: 10.1023/A:1009754219459.

Buforn, E., C. López-Sánchez, L. Lozano, J. M. Martínez-Solares, S. Cesca, C. S. Oliveira, and A. Udías (2020). Re-evaluation of seismic intensities and relocation of 1969 Saint Vincent Cape seismic sequence: A comparison with the 1755 Lisbon earthquake, *Pure Appl. Geophys.* **177,** 1781–1800, doi: 10.1007/s00024-019-02336-8.

Buforn, E., C. Pro, S. Cesca, A. Udías, and C. del Fresno (2011). The 2010 Granada, Spain, deep earthquake, *Bull. Seismol. Soc. Am.* **101,** 2418–2430, doi: 10.1785/0120110022.

Buforn, E., C. Pro, C. S. de Galdeano, J. V. Cantavella, S. Cesca, B. Caldeira, A. Udías, and M. Mattesini (2017). The 2016 south Alboran earthquake ($M_w = 6.4$): A reactivation of the Ibero-Maghrebian region? *Tectonophysics* **712/173,** 704–715, doi: 10.1016/j.tecto.2017.06.033.

Buforn, E., A. Udías, C. de Sanz Galdeano, and S. Cesca (2015). The 1748 Montesa (southeast Spain) earthquake. A singular event, *Tectonophysics* **664,** 139–153, doi: 10.1016/j.tecto.2015.09.005.

Buforn, E., A. Udías, and J. Mezcua (1988). Seismicity and focal mechanisms in South Spain, *Bull. Seismol. Soc. Am.* **78,** 2008–2024.

Clavero, J. L., C. Sanz de Galdeano, and R. Yus (2024). La evolución de las laderas de la Sierra de Alhama (provincias de Granada y Málaga). Influencia de la estructura geológica y la paleosismicidad, *Geogaceta* **75,** 63–66, doi: 10.55407/geogaceta100351 (in Spanish).

Convertito, V., and N. A. Pino (2014). Discriminating among distinct source models of the 1908 Messina Straits earthquake by modelling intensity data through full wavefield seismograms, *Geophys. J. Int.* **198,** 164–173, doi: 10.1093/gji/ggu128.

Cultrera, G., F. Pacor, G. Franceschina, A. Emolo, and M. Cocco (2009). Directivity effects for moderate-magnitude earthquakes (Mw 5.6–6.0) during the 1997 Umbria–Marche sequence, central Italy, *Tectonophysics* **476,** nos. 1/2, 110–120.

De Pro-Díaz, Y., H. Perea, J. M. Insua-Arévalo, J.J. Martínez-Díaz, and C. Canora (2023). Constraining earthquake fault sources through the use of intensity data and seismic scenarios: Application to the Betic Cordillera (South Spain), *Front. Earth Sci.* **11,** 1214836, doi: 10.3389/feart.2023.1214836.

Deschamps, A., Y. Gaudemer, and A. Cisternas (1982). The El Asnam, Algeria, earthquake of 10 October 1980: Multiple-source mechanism determined from long period records, *Bull. Seismol. Soc. Am.* **72,** 1111–1128.

Douville, R. (1906). Esquisse géologique des Préalpes subbétiques: partie centrale, *Thése de Doctorat*, Paris, France, 222 pp. (in French).

Douville, R. (1911). La Peninsule Iberique, in *Handbuch der regionalen Geologie*, C. Winter (Editor), Universitaetsbuchhandlung, Heidelberg, Germany, 175 pp. (in German).

Faenza, L., and A. Michelini (2010). Regression analysis of MCS intensity and ground motion parameters in Italy and its application in ShakeMap, *Geophys. J. Int.* **180,** 1138–1152.

Fernández de Castro, M., J. P. Lasala, D. Cortazar, and J. Gonzalo y Tarín (1885). *Terremotos de Andalucía. Informe de la comisión nombrada para su estudio dando cuenta del estado de los trabajos*, Imprenta de M. Tello, Madrid, Spain (in Spanish).

Fouqué, F. (1889a). Chap. 4, Tremblement de terre d'Andalousie 25 Decembre 1884, in *Les tremblements de terre*, J. B. Bailliere et fils (Editor), Paris, France (in French).

Fouqué, F. (1889b). Mission de l'Andalousie: Etude relatives au tremblement de terre du 25 decembre et à la constiution géologique du sol ébranlé par les secoursses, *Acad. Sci. Mem.* **XXX,** 1–772 (in French).

Galbis, J. (1932). *Catalogo Sísmico de la zona comprendida entre los meridianos 5º E y 20º W de Greenwich y los paralelos 45º y 25º N. vols. I y II*, Dirección General del Instituto Geográfico, Catastral y de Estadística, Madrid, Spain (in Spanish).

Galindo Zaldívar, J., A. J. Gil, M. J. Borque, C. LechadoMarín, P. Ruano, and C. Sanz de Galdeano (2004). The Zafarraya fault in the frame of the active tectonic structures of the central Betic Cordillera (southern Spain), *Proc. of the workshop COST-ACTION 625 "Actives faults: Analysis, processes and monitoring"*, L. Picardi and E. Tondi (Editors), Studi Geologici Camerti, 63–65.

Gallahue, M., and N. Abrahamson (2023). New methodology for unbiased ground-motion intensity conversion equations, *Bull. Seismol. Soc. Am.* **113,** 1133–1151, doi: 10.1785/0120220224.

Gasperini, P., F. Bernardini, G. Valensise, and E. Boschi (1999). Defining seismogenic sources from historical earthquake felt 1435 reports, *Bull. Seismol. Soc. Am.* **89,** 94–110.

Gasperini, P., G. Vannucci, D. Tripone, and E. Boschi (2010). The location and sizing of historical earthquakes using the attenuation of macroseismic intensity with distance, *Bull. Seismol. Soc. Am.* **100,** 2035–2066, doi: 10.1785/0120090330.

Gentil, P., and J. L. de Justo (1983). El Terremoto de Carmona de 1504, in *Sismicidad histórica de la región de la Península Ibérica*, As. Española de Ingeniería Sísmica, Madrid, Spain, 9–12 (in Spanish).

Goded, T., E. Buforn, and D. Muñoz (2008). The 1484 and 1680 Malaga (Southern Spain) earthquakes, *Seismol. Res. Lett.* **79,** 707–715, doi: 10.1785/gssrl.79.5.707.

Griffin, J., N. Nguyen, P. Cummins, and A. Cipta (2019). Historical earthquakes of the Eastern Sunda Arc: Source mechanisms and intensity-based testing of Indonesia's national seismic hazard assessment, *Bull. Seismol. Soc. Am.* **109,** 43–65, doi: 10.1785/0120180085.

Grünthal, G. (Editor) (1998). *European Macroseismic scale 1998*, Vol. 15, Cahiers du Centre Européen de Geodynamique et de Sismologie, Luxembourg.

Grützner, C., P. Ruano, A. Jabaloy, J. Galindo-Zaldívar, P. Heidmann-Becker, C. Sanz de Galdeano, A. Rudersdorf, and K. Reicherter (2013). Late Holocene rupture history of the Ventas de Zafarraya Fault (Southern Spain), *Cuaternario y Geomorfología* **27,** nos. 3/4, 5–32.

Heimann, S., M. Kriegerowski, M. Isken, S. Cesca, S. Daout, F. Grigoli, C. Juretzek, T. Megies, N. Nooshiri, A. Steinberg, *et al.* (2017). Pyrocko—An open-source seismology toolbox and library V.0.3, *GFZ Data Services*, doi: 10.5880/GFZ.2.1.2017.001.

Honoré, L., F. Courboulex, and A. Souriau (2011). Ground motion simulations of a major historical earthquake (1660) in the French Pyrenees using recent moderate size earthquakes, *Geophys. J. Int.* **187,** 1001–1018, doi: 10.1111/j.1365-246X.2011.05193.x.

Hough, S. E., and R. Bilham (2024). The 1886 Charleston, South Carolina, earthquake: Intensities and ground motions, *Bull. Seismol. Soc. Am.* **114,** 1658–1679, doi: 10.1785/0120230224.

Hough, S. E., and R. W. Graves (2020). The 1933 Long Beach earthquake (California, USA): Ground motions and rupture scenario, *Sci. Rep.* **10,** 10017, doi: 10.1038/s41598-020-66299-w.

Hough, S. E., R. Bilham, N. Ambraseys, and N. Feldl (2005), Revisiting the 1897 Shillong and 1905 Kangra earthquakes in northern India: Site response, Moho reflections and a triggered earthquake, *Curr. Sci.* **88,** 10, 1632–1638.

Hough, S. E., S. S. Martin, S. J. Symithe, and R. Briggs (2022). Rupture scenarios for the 3 June 1770 Haiti earthquake, *Bull. Seismol. Soc. Am.* **113,** 157–185, doi: 10.1785/0120220108.

López-Arroyo, A., A. J. Martín Martín, and J. Mezcua (1981). Terremoto de Andalucía. Influencia en sus efectos de las condiciones del terreno y tipo de construcción, En: *El terremoto de Andalucía del 25 de Diciembre de 1884*, Monografía Instituto Geográfico Nacional, Madrid, Spain, 5–94 (in Spanish).

López-Sánchez, C., E. Buforn, S. Cesca, L. Lozano, C. Sanz de Galdeano, M. Mattesini, A. Udías, and J. V. Cantavella (2022). Intermediate-depth earthquakes in southern Spain and Alboran Sea, *Tectonophysics* **825,** doi: 10.1016/j.tecto.2022.229238.

Lozos, J. C. (2016). A case for historic joint rupture of the San Andreas and San Jacinto faults, *Sci. Adv.* **2,** e1500621, doi: 10.1126/sciadv.1500621.

Lucas, M. C., S. E. Hough, S. Stein, L. Salditch, M. M. Gallahue, J. S. Neely, and N. Abrahamson (2023). Uncertainties in intensity-based earthquake magnitude estimates, *Seismol. Res. Lett.* **94,** 2202–2214, doi: 10.1785/0220230030.

Ma, J., L. Dong, G. Zhao, and X. Li (2019). Ground motions induced by mining seismic events with different focal mechanisms, *Int. J. Rock Mech. Mining Sci.* **116,** 99–110.

Madarieta-Txurruka, A., L. González-Castillo, J. A. Peláez, J. Galindo-Zaldívar, M. J. Borque, M. C. Lacy, A. M. Ruiz-Armenteros, J. Henares, P. Ruano, A. Sánchez-Alzola, *et al.* (2024). Active shortening simultaneous to normal faulting based on GNSS, geophysical, and geological data: The seismogenic Ventas de Zafarraya Fault (Betic Cordillera, southern Spain), *Tectonics* **43,** doi: 10.1029/2023TC007956.

Martín, A. J. (1984). Riesgo Sísmico en la Península Ibérica, *Tesis Doctoral*, Universidad Politécnica de Madrid, Vol. I and II, Talleres del Instituto Geográfico Nacional, Madrid, Spain (in Spanish).

Martin, S. S., and S. E. Hough (2022). The 8 April 1860 Jour de Pâques earthquake sequence in Southern Haiti, *Bull. Seismol. Soc. Am.* **112,** 2468–2486, doi: 10.1785/0120220016.

Martínez-Solares, J. M., and A. López-Arroyo (2004). The great historical 1755 earthquake. Effects and damage in Spain, *J. Seismol.* **8,** 275–294.

Martínez-Solares, J. M., and J. Mezcua (2002). *Catalogo sísmico de la península Ibérica (880 a.C.-1900)*, Monografía 18, Instituto Geográfico Nacional, Madrid, Spain (in Spanish).

Masi, A., L. Chiauzzi, G. Nicodemo, and V. Manfredi (2020). Correlations between macroseismic intensity estimations and ground motion measures of seismic events, *Bull. Earthq. Eng.* **18,** 1899–1932, doi: 10.1007/s10518-019-00782-2.

Medvedev, S., W. Sponheuer, and V. Karník (1964). Neue seismische Skala Intensity scale of earthquakes, 7. Veröff. Institut für Bodendynamik und Erdbebenforschung in Jena, in *Tagung der Europäischen Seismologischen Kommission vom 24.9. bis 30.9.1962, in Jena*, Vol. 77, Deutsche Akademie der Wissenschaften zu, Berlin, Germany, 69–76 (in German).

Mezcua, J., J. Rueda, and G. R. Blanco (2013). Iberian Peninsula historical seismicity revisited: An intensity data bank, *Seismol. Res. Lett.* **84,** no. 1, 9–18, doi: 10.1785/0220120097.

Mezcua, J., J. Rueda, and R. M. García Blanco (2004). Reevaluation of historic earthquakes in Spain, *Seismol. Res. Lett.* **7,** 75–81, doi: 10.1785/gssrl.75.1.75.

Mezcua, J., J. Rueda, and R. M. García Blanco (2020). Characteristics of a new regional seismic–intensity prediction equation for Spain, *Nat. Hazards* **101,** 817–832, doi: 10.1007/s11069-020-03897-x.

Mudarra-Hernández, M., J. C. Mosquera-Feijoo, and E. Sanz-Pérez (2023). Numerical simulation and characterization of the hydromechanical alterations at the Zafarraya Fault due to the 1884 Andalusia earthquake (Spain), *Water* **15,** no. 5, 850, doi: 10.3390/w15050850.

Munafò, I., A. Akinci, M. Taroni, L. Faenza, I. Oliveti, A. Antonucci, A. A. Gomez-Capera, and A. Rovida (2024). Studying past earthquakes with modern techniques: Ground-motion simulations for the 11 January 1693 Noto earthquake in Italy, *Seismol. Res. Lett.* **95,** 3387–3405, doi: 10.1785/0220240105.

Muñoz, D., and A. Udías (1991). Three large historical earthquakes in Southern Spain, in *Seismicity, Seismotectonics and Seismic Risk of the Ibero-Maghrebian Region*,J. Mezcua and A. Udías (Editors), Monografía n. 8, Instituto Geográfico Nacional, Madrid, Spain, 175–182.

Murphy, J. R., and I. J. O'Brien (1977). The correlation of peak ground acceleration amplitude with seismic intensity and other physical parameters, *Bull. Seismol. Soc. Am.* **67,** 877–915.

Murphy Corella, P. (2020). *Los terremotos de Almería de 1804 en el Archivo Histórico Nacional*, Instituto Geográfico Nacional, CNIG, Madrid, Spain, available at https://www.ign.es/web/ign/portal/libros-digitales/terremotos-almeria-1804 (last accessed June 2025) (in Spanish).

Oliveti, I., L. Faenza, and A. Michelini (2022). New reversible relationships between ground motion parameters and macroseismic intensity for Italy and their application in ShakeMap, *Geophys. J. Int.* **231,** 1117–1137, doi: 10.1093/gji/ggac245.

Orueta y Duarte, D. (1885). *Informe sobre los terremotos ocurridos en el sud de España en Diciembre de 1884 y Enero de 1885*, Tip. De Fausto Muñoz, Málaga, Spain (in Spanish).

Reicherter, K. R., A. Jabaloy, J. Galindo-Zaldívar, P. Ruano, P. Becker-Heidmann, J. Morales, S. Reiss, and F. González-Lodeiro (2003). Repeated palaeoseismic activity of the Ventas de Zafarraya fault (S Spain) and its relation with the 1884 Andalusian earthquake, *Int. J. Earth Sci.* **92,** 912–922, doi: 10.1007/s00531-003-0366-3.

Rodríguez-Peces, M. J., J. García-Mayordomo, J. M. Azañón, J. M. Arévalo Insua, and J. Jimenez Pintor (2011). Constraining pre-instrumental earthquake parameters form slope stability back analysis: Paleosismic reconstructionof the Güevejar landslide during the 1st November 1755 and 25th December 1884 Arenas del Rey earthquake, *Quaternary Int.* **242,** 76–89, doi: 10.1016/j.quaint.2010.11.027.

Sanz de Galdeano, C. (1983). Los accidentes y fracturas principales de las Cordilleras Béticas, *Estud. Geol.* **39,** 157–165 (in Spanish).

Sanz de Galdeano, C. (1985). La fracturación del borde sur de la depresión de Granada (Discusión del escenario del terremoto del 25–XII–1884), *Estud. Geol.* **41,** 59–68 (in Spanish).

Sanz de Galdeano, C. (2013). The Zafarraya Polje (Betic Cordillera, Granada, Spain), a basin open by lateral displacement and bending, *J. Geodynam.* **64,** 62–70, doi: 10.1016/j.jog.2012.10.004.

Sanz de Galdeano, C., and P. Alfaro. (2004). Tectonic significance of the present relief of the Betic Cordillera, *Geomorphology* **63,** 178–190.

Sanz de Galdeano, C., J. Mera-Prieto, and B. Andreo (2019). Structure of the Alpujarride Complex and hydrogeological observations to the NW of Sierra Tejeda (Granada and Malaga provinces, Betic Internal Zone, Spain), *Estud. Geol.* **75,** no. 1, doi: 10.3989/egeol.43395.509.

Seekins, L. C., and J. Boatwright (2010). Rupture directivity of moderate earthquakes in northern California, *Bull. Seismol. Soc. Am.* **100,** 1107–1119.

Steikhardt, L. (1932). Die Erdbebentágíigkeit am Westrand des Mittelmeeres und ihre Geologische Bedeutung, *Doktor Dissertation*, Thüringischer Landuniversität Jena, Jena, Germany (in German).

Stich, D., F. L. Mancilla, D. Baumont, and J. Morales (2005). Source analysis of the Mw 6.3 Al Hoceima earthquake (Morocco) using regional apparent source time functions, *J. Geophys. Res.* **110,** doi: 10.1029/2004JB003366.

Sun, J., Y. Yu, and Y. Li (2018). Stochastic finite-fault simulation of the 2017 Jiuzhaigou earthquake in China, *Earth Planets Space* **70,** 128, doi: 10.1186/s40623-018-0897-2.

Taramelli, T., and G. Mercalli (1885). *Il terremoto andalusí comiciati il 25 Decembre 1884*, Serie Quarta, 1885, III, Real Accademia dei Lincei, Rome, Italy, 116–222 (in Italian).

Udías, A., and D. Muñoz (1979). The Andalusian earthquake of 25 December 1884, *Tectonophysics* **53,** 291–299, doi: 10.1016/0040-1951(79)90074-X.

Udías, A., E. Buforn, and M. Mattesini (2022). Contemporary publications in Europe on the Spanish earthquake of 1884, *Seismol. Res. Lett.* **93,** 3489–3497, doi: 10.1785/0220220176.

Vannucci, G. (2024). Analysis of the macroseismic cumulative damage in the seismic sequences in Italy, *Bull. Earthq. Eng.* **23,** 759–778, doi: 10.1007/s10518-024-02073-x.

Vannucci, G., P. Gasperini, B. Lolli, and L. Gulia (2019). Fast characterization of sources of recent Italian earthquakes from macroseismic intensities, *Tectonophysics* **750,** 70–92, doi: 10.1016/j.tecto.2018.11.002.

Vannucci, G., B. Lolli, and P. Gasperini (2021). Inhomogeneity of macroseismic intensities in Italy and consequences for macroseismic magnitude estimation, *Seismol. Res. Lett.* **92,** 2234–2244, doi: 10.1785/0220200273.

Vidal, F. (1986). Sismotectónica de la región Béticas-Mar de Alborán, *Ph.D. Dissertation*, Universidad de Granada, Granada, Spain (in Spanish).

Vidale, J. E. (1989). Influence of focal mechanism on peak accelerations of strong motions of the Whittler Narrows, California, earthquake and aftershock, *J. Geophys. Res.* doi: 10.1029/JB094iB07p09607.

Wells, D. L., and K. J. Coppersmith (1994). New empirical relationships among magnitude, rupture length, rupture width, rupture area, and surface displacement, *Bull. Seismol. Soc. Am.* **84,** 974–1002.

Xie, J., P. Zimmaro, X. Li, and Z. Wen (2017). Rupture directivity effects on strong ground motion during the 15 April 2016 MW 7.0 Kumamoto earthquake in Japan, *Bull. Seismol. Soc. Am.* **107,** 1265–1276.

Manuscript received 28 January 2025
Published online 26 June 2025